Acta Oceanol. Sin., 2020, Vol. 39, No. 7, P. 79–90
https://doi.org/10.1007/s13131-020-1596-y
http://www.hyxb.org.cn
E-mail: hyxbe@263.net

Observation of an anti-cyclonic mesoscale eddy in the subtropical northwestern Pacific Ocean from altimetry and Argo profiling floats

Yang Wang[1, 2], Cheng Li[3, 4*], Qingyu Liu[1]

[1] School of Marine Science and Technology, Northwestern Polytechnical University, Xi'an 710072, China

[2] Maritime Environment Construction Office, Beijing 100081, China

[3] Guangdong Key Laboratory of Coastal Ocean Variability and Disaster Prediction, College of Ocean and Meteorology, Guangdong Ocean University, Zhanjiang 524088, China

[4] Marine Resources Big Data Center of South China Sea, Southern Marine Science and Engineering Guangdong Laboratory (Zhanjiang), Zhanjiang 524025, China

Received 25 September 2019; accepted 4 February 2020

Abstract

The comprehensive three-dimensional structures of an anti-cyclonic mesoscale eddy (AE) in the subtropical northwestern Pacific Ocean were investigated by combining the Argo floats profiles with enhanced vertical and temporal sampling and satellite altimetry data. The AE originated near the Kuroshio Extension and then propagated westward with mean velocity of 8.9 cm/s. Significant changes and evolutions during the AE's growing stage (T1) and further growing stage (T2) were revealed through composite analysis. In the composite eddy core, maximum temperature (T) and salinity (S) anomalies were of 1.7 (1.9)°C and 0.04 (0.07) psu in T1 (T2) period, respectively. The composite T anomalies showed positive in almost whole depth, but the S anomalies exhibited a sandwich-like pattern. The eddy's intensification and its influence on the intermediate ocean became more significant during its growth. The trapping depth increased from 400×10^4 Pa to 580×10^4 Pa while it was growing up, which means more water volume, heat and salt content in deeper layers can be transported. The AE was strongly nonlinear in upper oceans and can yield a typical mean volume transport of 0.17×10^6 m^3/s and a mean heat and salt transport anomaly of 3.6×10^{11} W and -2.1×10^3 kg/s during the observation period. The Energy analysis showed that eddy potential and kinetic energy increased notably as it propagated westward and the baroclinic instability is the major energy source of the eddy growth. The variation of the remained Argo float trapped within the eddy indicated significant water advection during the eddy's propagation.

Key words: mesoscale eddy, three-dimensional structure, volume transport, available heat and salt content anomaly, energy analysis

Citation: Wang Yang, Li Cheng, Liu Qingyu. 2020. Observation of an anti-cyclonic mesoscale eddy in the subtropical northwestern Pacific Ocean from altimetry and Argo profiling floats. Acta Oceanologica Sinica, 39(7): 79–90, doi: 10.1007/s13131-020-1596-y

1 Introduction

Oceanic eddies are a kind of vortices in qusi-geostrophic balance or gradient wind balance and most of them have long lifetime and horizontal scales of about 10–100 km and can effectively transport diverse tracers (Wunsch, 1999; Wang et al., 2001; Morrow et al., 2003; Chelton et al., 2011a; Zhang et al., 2015, 2019; Li et al., 2017). Among the different size of eddies, the mesoscale ones or mesoscale eddies with the typical horizontal scale of ~100 km have been widely studied using altimeter-based eddy identification and tracking criterions (Roemmich and Gilson, 2001; Chelton et al., 2007, 2011b; Chaigneau et al., 2008, 2011; Liu et al., 2012; Yang et al., 2013; Zhang et al., 2014). Spatial and temporal variations of kinetic energy of mesoscale eddies were investigated in global or regional oceans (Qiu, 1999; Noh et al., 2007; Qiu and Chen, 2010; Yoshida et al., 2011). Furthermore, based on eddy-targeted shipboard or moored or Argo observations, the three-dimensional structure and material transport associated with mesoscale eddies were also reported by previous literatures (Liang et al., 2012; Zhang et al., 2013, 2016; Chu et al., 2014; Yang et al., 2013; Sun et al., 2017).

Statistical descriptions of eddy activities based on satellite altimetry observations reveal that mesoscale eddies are particularly active in the subtropical northwestern Pacific Ocean (STNWP)（Qiu, 1999; Qiu and Chen, 2010, 2013） and they have been extensively studied. Previous studies in this region indicate that mesoscale eddies are of great importance for modulating the background currents (Zhang et al., 2001; Yuan and Wang, 2011; Zheng et al., 2011), the water mass transport and re-distribution (Roemmich and Gilson, 2001; Qiu and Chen, 2005; Rudnick et al., 2011; Li and Wang, 2012) and even diapycnal mixing (Jing et al., 2011). But most previous works on mesoscale eddy in the NWP made emphasis on the eddy kinetic energy (EKE) variabilities

Foundation item: The National Program on Global Change and Air-Sea Interaction under contract No. GASI-IPOVAI-01-02; the program for scientific research start-up funds of Guangdong Ocean University under contract No. R19011; the fund of Southern Marine Science and Engineering Guangdong Laboratory (Zhanjiang) under contract No. ZJW-2019-08.
*Corresponding author, E-mail: xiaoxianglch@163.com

(Qiu, 1999; Noh et al., 2007; Qiu and Chen, 2010; Liu et al., 2012) and regional composite analysis of the three-dimensional eddy structures (Yang et al., 2013; Sun et al., 2017). However, the observational analysis focused on a specific eddy and the associated changes and evolutions during its growth is rare in the NWP.

With the help of sea surface height (SSH) measured by satellite altimeter, considerable advancements has been made in researching the surface expression of mesoscale eddies, but the subsurface eddy structures are still not well known, which is of great importance in exploring eddy dynamics and evaluating eddy-induced water mass transport (Qiu and Chen, 2010; Roemmich and Gilson, 2001; Qiu and Chen, 2005; Xiu et al., 2012; Chen et al., 2012). Combining Argo floats profiles and satellite altimetry data, composite analysis of mesoscale eddy was adopted in different regional studies (Roemmich and Gilson, 2001; Chaigneau et al., 2011; Yang et al., 2013; Zhang et al., 2014; Sun et al., 2017). These studies provide robust three-dimensional images of temperature (T), salinity (S) and velocity of the mesoscale eddy and also reveal the heterogeneity of the eddy extents. Particularly, Zhang et al. (2014) makes a description of the universal structure of global mesoscale eddy with simple analytical functions. Furthermore, mesoscale eddies have potentially significant influences on the regional ocean dynamics because they correspond with T/S anomalies induced by vertical fluctuations which can deeply influence remote seas through ocean circulations (Zhang et al., 1998; Sasaki et al., 2010; Li et al., 2012). Thus, one important purpose of this work is to construct the three-dimensional structures of the observed anti-cyclonic mesoscale eddy (AE) with T/S data profiles from the deployed Argo floats (with a high-time-resolution sampling) and examine its evolution during different stages of eddy growth. According to the previous studies, the nonlinear eddies play an important role in modulating the transport of the Kuroshio and water exchanging between the STNWP and the marginal seas (Zhang et al., 2001; Zheng et al., 2008, 2011; Yuan and Wang, 2011; Hu et al., 2012), which are indispensable in both local ocean circulation and large-scale water mass exchange. Therefore, the second purpose of this study is to estimate the eddy-induced water volume, heat and salt transport during the different stages of eddy growth. The distributions of the Argo floats relative to the eddy centers and the energy analysis during the eddy's different stages of growth were examined. Depended on the variation of the remained trapped Argo floats, the transport efficiency of the original water mass can also be estimated.

This paper is organized as follows. Section 2 describes the data sources and methods of automated eddy identifying/tracking and composition of the eddy. Section 3 demonstrates the three-dimensional structures of the AE composed in two eddy-proceeding periods with Argo data profiles; gives the eddy-induced volume, heat and salt transport and the eddy energy analysis. Section 4 discusses the estimated transport efficiency during the eddy's growth and the variability of Argo floats' distributions relative to the eddy center. In the end, the main contents of this paper are summarized in Section 5.

2 Data and methods

2.1 *Satellite altimeter data*

In order to identify and track the mesoscale eddy, the daily sea level anomaly (SLA) data from the multi-satellite AVISO product (http://marine.copernicus.eu/) between March and July 2014 and the corresponding geostrophic velocity data were utilized. Both the SLA and surface geostrophic velocity were bilinearly interpolated onto a 1/4°×1/4° and 1/3×1/3° gridded map, respectively.

2.2 *Argo profiling floats data*

The three-dimensional structure of the AE was investigated using T/S profiles from Argo-profiling floats (Fig. 1b) with enhanced vertical and temporal sampling (World Meteorological Organization (WMO) IDs 2901550–2901566), which were deployed within the AE during 25 and 26 March 2014 (available at http://www.usgodae.org and http://www.argo.org.cn.). The Argo profiles used in the paper are deployed by the targeted field (Fig. 1a) experiment P-MoVE (Pacific Mode water Ventilation Experiment), which made the first direct observations of eddy subductions processes in the western North Pacific (Xie, 2013; Xu et al., 2016). The Argo profiles from 27 March to 30 July 2014 were investigated in this study. These Argo floats park at 500 m, and record T, S and pressure from 1 000 m to the sea surface within one day. The Argo floats measure data mostly synchronously, and they can arrive at the surface within 30 min difference. The vertical sampling interval of the profiles is 2 m above 600 m and 10 m below it. Only Argo profiles with good quality were obtained and then all of them were interpolated onto a 1 m vertical grid for further analysis.

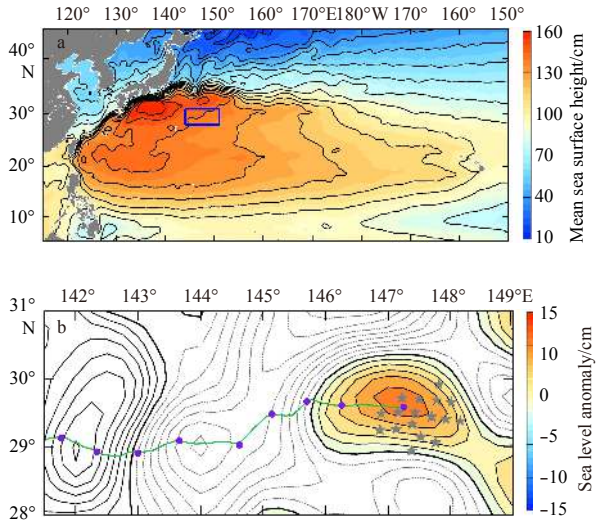

Fig. 1. Mean sea surface height (cm) of the northwestern Pacific Ocean from Rio et al. (2009) the contour interval is 10 cm and the blue rectangle indicates the regions where the anti-cyclonic eddy (AE) was observed (a), and the locations of the Argo floats (gray stars) deployed in the blue rectangle (b). The contours denote the altimeter sea level anomaly (SLA) field on that day. The contour interval of the SLA is 2 cm, and the negative, zero, and positive values are marked by the gray dashed, thick solid, thin solid lines, respectively. The green solid line denotes the trajectory of the AE and the purple dots' interval is two weeks.

2.3 *Identification of the mesoscale eddy*

The Okubo-Weiss (Okubo, 1970; Weiss, 1991) method was used to detect mesoscale eddies. The Okubo-Weiss parameter W is defined as:

$$W = S_n^2 + S_s^2 - \omega^2, \tag{1}$$

where ω, S_n and S_s denote vertical component of relative vorticity, the strain and shear deformation, respectively.

$$\omega = \frac{\partial v'}{\partial x} - \frac{\partial u'}{\partial y}, S_n = \frac{\partial u'}{\partial x} - \frac{\partial v'}{\partial y}, S_s = \frac{\partial v'}{\partial x} + \frac{\partial u'}{\partial y}, \quad (2)$$

where u' and v' represent geostrophic velocity anomalies calculated based on the geostrophic relation. The criterion: W<–0.2σ_W was used to identify mesoscale eddy in this paper, where σ_W denotes the standard deviation of W in the given region. The mean coordinates within the eddy was defined as the eddy center. And the equivalent radius of the eddy was represented by the radius of an equal-area circle. Then the whole information of the detected eddy can be obtained at each time step.

2.4 *Construction of the Composite AE*

According to Section 2.3, the eddy center and radius can be given at each day. Thus, the spatial distribution of every property (T, S, density) within the eddy can be constructed through composite analysis with a coordinate system (Δdx, Δdy) in which each Argo profile is situated to its corresponding eddy center (Δdx=Δdy=0). We firstly calculated the distances (D) between the locations of Argo profile and the eddy center at each day. Since the continuous variation of the eddy size, the distances are scaled based on $D_n = D \cdot \frac{\overline{R}}{R}$, where R denotes the instantaneous eddy radius and $\overline{R}$ denotes mean eddy radius (Zhang et al., 2013). The values of eddy radius were almost less than 190 km, thus only the profiles located less than 190 km away from the eddy center were analyzed. Then every property were transformed into the new coordinate system (Δdx, Δdy) and projected onto 10 km×10 km grids based on the objective cressman interpolation at each layer. This grid spacing was chosen for the minimum distances between two profiles were almost less than 10 km. At each vertical level, the dynamic height (DH) relative to the 1 000 m reference depth was also computed, which is a common level adopted in previous studies (Chaigneau et al., 2011; Yang et al., 2013). Finally, to better describe the mesoscale perturbations captured by the floats, anomalies of every property (T',S',DH') were computed by removing climatological profiles and further processed through the composite analysis as mentioned above. Here, the climatological T/S profiles were obtained by interpolating the WOA13 to floats' positions and times. To investigate the internal changes during the growth of the eddy, the composite analysis of the AE were made separately within two periods: the eddy growing stage T1 (27 March to 30 May) and the eddy further growing stage T2 (21 May to 30 July).

3 Results

3.1 *General features of AE's evolution*

Figure 2 shows the evolution of the AE detected from the geostrophic velocity anomalies as well as the SLA data. The AE originated on 25 March near the Kuroshio Extension (Fig. 1b) and then propagated westward because of the beta effect. The mean propagating speed of the AE is 9.7 (8.0) cm/s in T1 (T2) period. The time series of radius, amplitude and EKE of the eddy are shown in Fig. 3. Following Oey (2008), the EKE was defined as

$$\mathrm{EKE} = (u'^2 + v'^2)/2, \quad (3)$$

and it is averaged within the detected eddy boundary. During its early two months, the radius fluctuated between 70 and 80 km. The eddy's radius increased gradually and reached its maximum

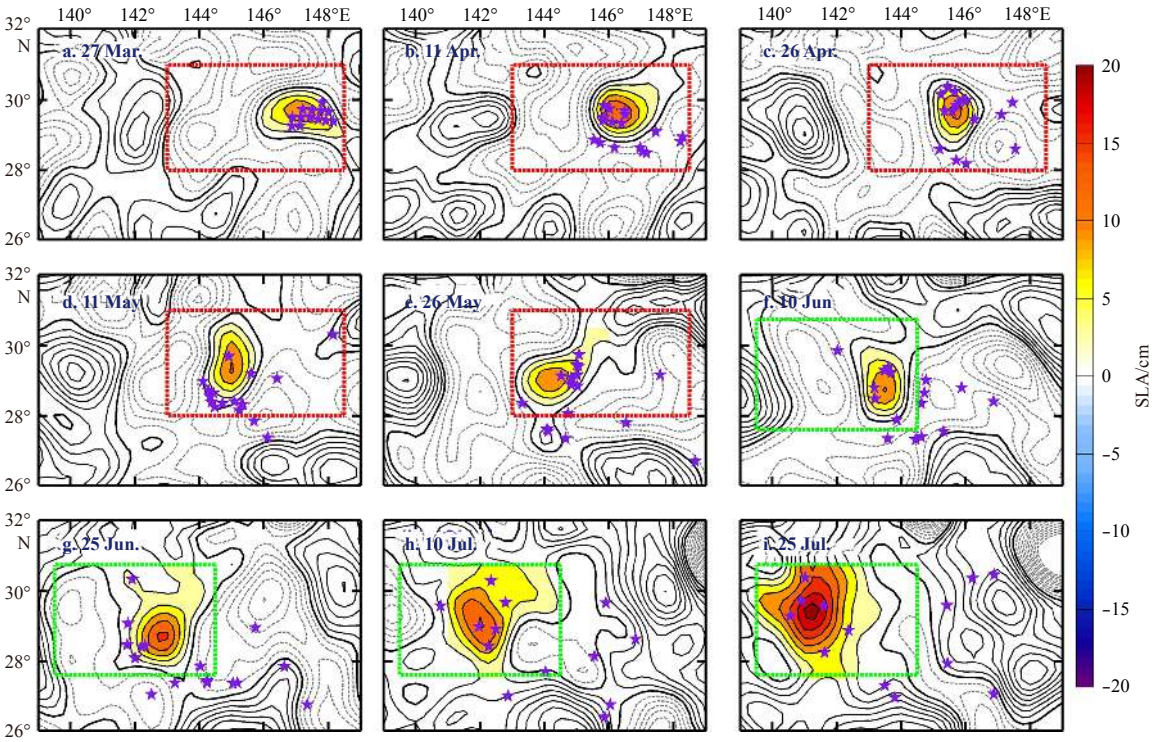

Fig. 2. Evolutions of the AE detected by altimeter SLA from March 27 to July 25, 2014. The contours denote the altimeter SLA field on that day. The contour interval of the SLA is 3 cm, and the negative, zero, and positive values are marked by the gray dashed, thick solid, thin solid lines, respectively. The purple stars denote the locations of the Argo floats. The gray rectangle denotes the field of AE during T1 period; the red rectangle denotes the field of AE during T2 period.

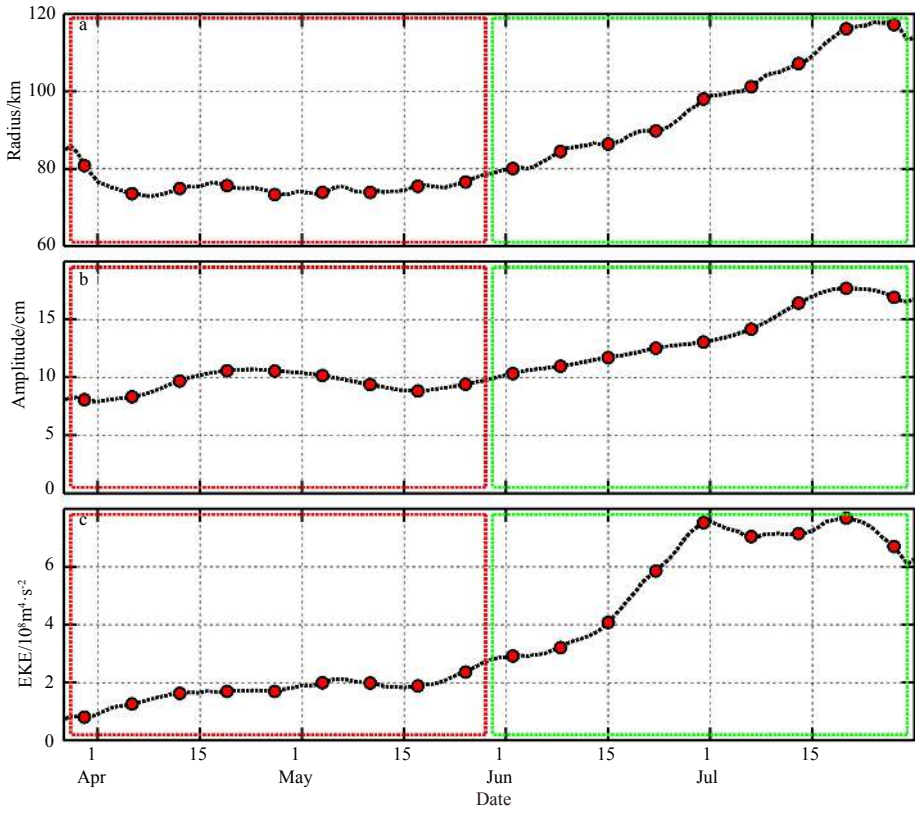

Fig. 3. Daily evolution of radius (a), amplitude (b) , EKE (c) of the AE. The red and green rectangles indicate the T1 and T2 period, respectively.

of 118 km in the following two months. The eddy amplitude varied similarly with the radius, fluctuating between 8 and 10.8 cm in the early stage, greatly increased to the maximum of 17.7cm and then decayed. The surface EKE of the AE kept an upward tendency especially from April to June and reached to the maximum at the end of the June. During the eddy growth, it is found that during the first half, the eddy radius, amplitude and EKE remain stable, but in the second half the eddy begin to grow rapidly. All of these properties variances indicated the significant intensification of AE during its growth.

3.2 *Three-dimensional eddy structures*

3.2.1 *T structures*

The vertical profiles of T' (maximum within the eddy core) were shown in Fig. 4a. According to Chaigneau et al. (2011), the eddy core was defined within the closed DH' contour which is associated with the strongest average swirl velocity of the composite eddy. The composite AE induced an overall warming in the entire observed depth except the upper layers, which was especially prominent (T'>1.6°C) in the main thermocline in both of the two periods. It showed that the main thermocline of the composite AE was anomalously concave, because of its downward vertical movements near the eddy centers, which can be clearly found in the vertical sections of the potential density at Δdy=0 (Figs 7c and d). The composite AE represented a maximum T' of about 1.7 (1.9)°C centered at 490 (485)×10^4 Pa in T1 (T2). Although the mean T' greater than 1°C extend between 350×10^4 and 700 ×10^4 Pa, we still found weak T' of 0.26 (0.34)°C at 900 ×10^4 Pa in T1 (T2) period. All these features were also clearly represented in the vertical sections of T' at Δdy=0 across the composite AE (Figures not shown). The vertical profiles (Fig. 4c) and vertical sections at Δdy=0 (Figs 7c and d) of the density anomaly showed a core centered at around 500×10^4 Pa reached to its maximum of 0.18 kg/m^3 and 0.24 kg/m^3 in T1 and T2 period. Horizontal fields of T' at typical levels provided further insights into the eddy's T structure (Fig. 5). The composite AE showed a maximum T' with magnitude >1.2 (1.5)°C near the eddy centers between 450×10^4 to 600 ×10^4 Pa in T1 (T2) period. In addition, the anomaly magnitudes were relatively small below 750×10^4 Pa. The warming centers can be easily identified at each depth. The eddy structures in the upper layer were irregular in both T1 and T2 period, which was supposed to be related with the climatic cold T'. The maximum T' of the observed AE was comparable with previous results in the study region (Liu et al., 2012; Yang et al., 2013) The major difference is that the maximum T' of the mesoscale eddy were around at 200 m in the previous results of, but our observed AE was much deeper reaching 500 m.

3.2.2 *S structures*

The vertical profiles of S' (maximum within the eddy core) were shown in Fig. 4b. Generally speaking, the S' induced by AE exhibited an interesting sandwich-like pattern with two parts of negative anomalies separated by positive anomalies at about 320×10^4–650×10^4 Pa. The maximum of S' can reach to 0.04 (0.07) psu in T1 (T2) period. This structure was also clearly represented in the vertical sections of S' at Δdy=0 across the composite AE (figures not shown). The vertical distribution of the salinity shows a sandwich-like pattern, and at the surface the salinity anomaly was negative, which remind us there should be much fresh wa-

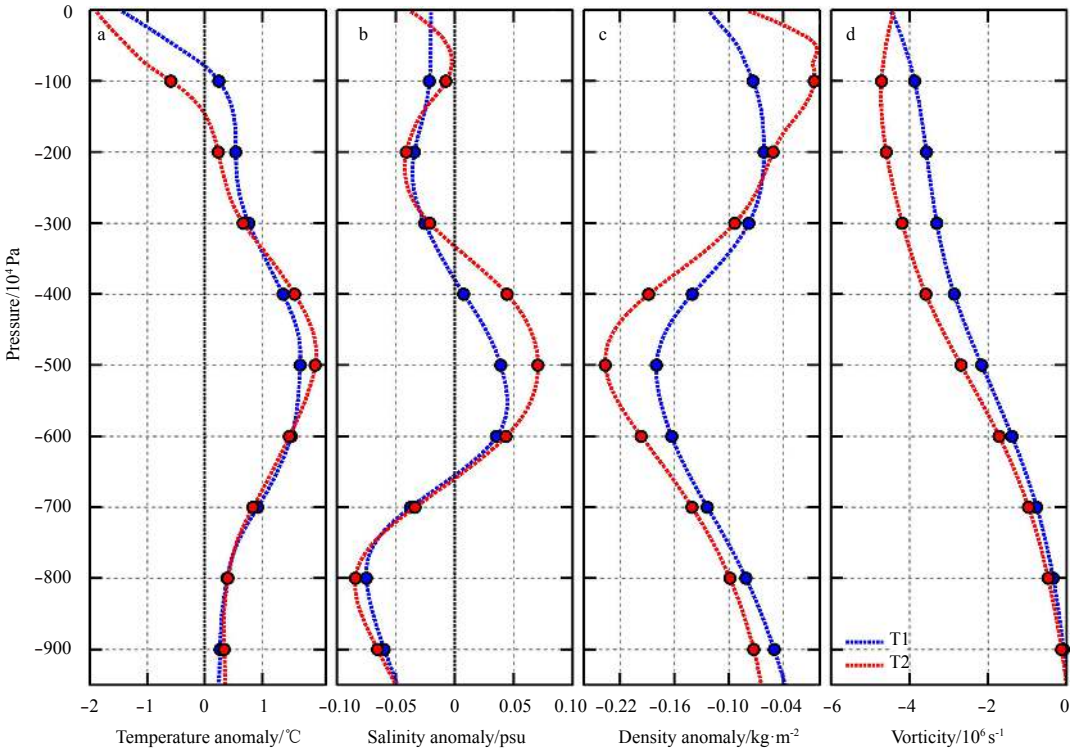

Fig. 4. Vertical profiles of temperature anomaly (a), salinity anomaly (b), density anomaly (c), and vorticity (maximum within the eddy core) (d) inside the composite AE. The blue (red) lines denote the values in T1 (T2) period.

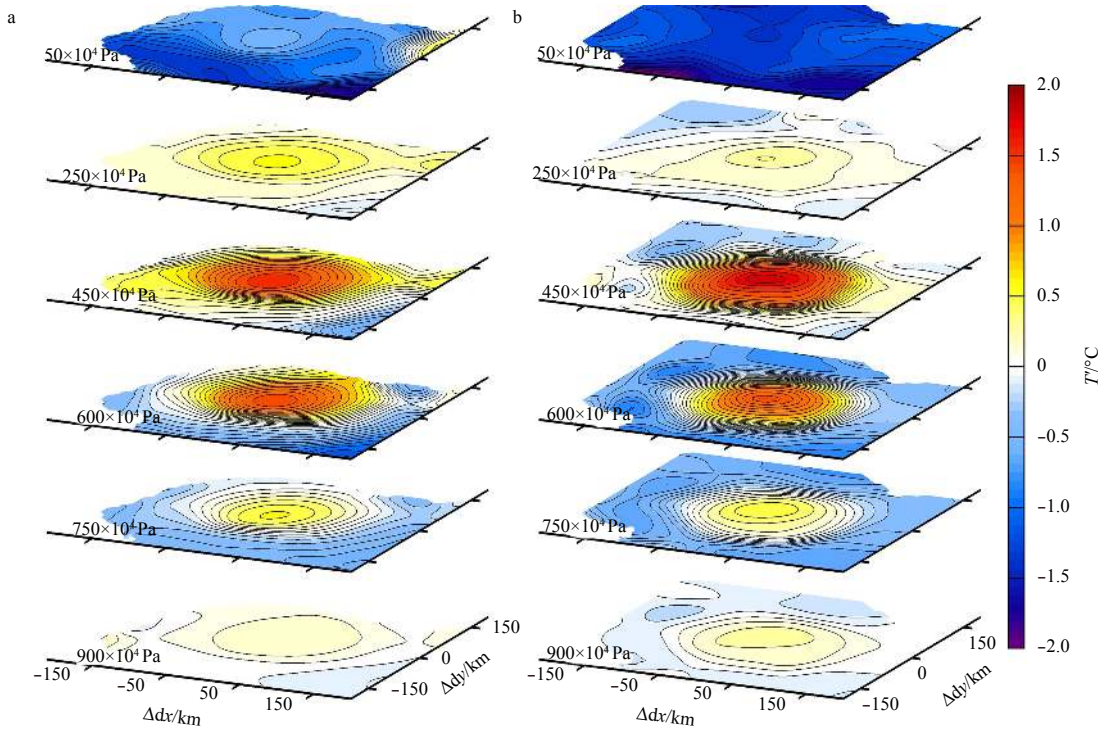

Fig. 5. T' fields (°C) of the composite AE at 50×10^4, 250×10^4, 450×10^4, 600×10^4, 750×10^4 and 900×10^4 Pa during periods T1 (a) to T2 (b). The contour interval is 0.01°C and the units of the X-axes (Δdx) and Y-axes (Δdy) are both kilometer.

ters on the surface probably induced by precipitation. At first, the distributions of main water masses in the study region were briefly examined. There are two important water masses: the subsurface high-salinity North Pacific Tropical Water (NPTW) (Suga et al., 2000) and the low-salinity North Pacific Intermediate Water (NPIW) (Talley, 1993). The most striking modification

of NPTW in the study region is its prominent freshening, which is more prominent in the surface ocean due to intensive diapycnal mixing with fresh surface water formed under the heavy precipitation (Qu et al., 1999; Li and Wang, 2012). It also demonstrated that the eddy T/S patterns are essentially determined by the water mass stratification. Therefore, it was suggested that the surface freshwater from the heavy rainfall (Qu et al., 1999; Li and Wang, 2012) subducted and formed the negative S' between 100×10^4 and 350×10^4 Pa. Then the NPTW and NPIW were in turn lowered by the downward motions of the AE, making the formation of the positive S' between 350×10^4 and 650×10^4 Pa and the weak negative S' below 650×10^4 Pa, separately. The horizontal S' fields (shown in Fig. 6) were relatively irregular compared with the T' fields, the eddy centers were not discernable in some layers, especially in T2 period. This is probably due to the differences between the background T and S fields (Yang et al., 2013) and small-scale process in this region, such as thermohaline intrusions can also disorder the S field (Rudnick et al., 2011; Li and Wang, 2012. The observed AE was just situated between the Kuroshio extension region and the subtropical region. Compared with previous studies, the S' structure of the observed AE showed more similar pattern with the composite eddies in the subtropical region with a sandwich-like structure (Liu et al., 2012; Yang et al., 2013). However, their difference is that the observed AE showed larger vertical content of surface fresh water reaching 300 m compared with previous results of only 100 m.

3.2.3 *Velocity structures*

The vertical sections of the composite geostrophic current velocity anomaly V' at Δdy=0 were shown in Figs 7a and b. It was clearly discernable that the AE greatly intensified in velocities from T1 to T2 period. In T1 period, V' was generally smaller than 0.13m/s. As time went on, V' exceeded 0.18 m/s in the surface and still reached to 0.13 m/s at the intermediate-layer depths in T2 period, which was even comparable with the surface V' magnitude in T1 period. The maximum V' was observed in the upper 0–100 m layer for T1 period and 0–200 m for T2 period. Compared the velocity fields between T1 and T2 period, it was discernable that the eddy's influence on the subsurface ocean was even more significant with its growth. These features were also clearly represented in the horizontal images shown in Fig. 8. Combining with the vertical distributions of the eddy vorticity (Fig. 4d), which was defined as the maximum vorticity within the eddy core, it was found that the growth and intensification of AE is significant between the two growth phase of the eddy.

3.3 *Eddy-induced volume transport*

In Sections 3.2, the three-dimensional structure of the AE was relatively well described with the combination of altimetry data and Argo profiles. Then the AE's contribution to volume, heat and salt transport can be further estimated based on its three-dimensional structure. The water volume can be effectively transported within the eddy core only when the eddy is sufficiently nonlinear, which means the rotational speed should exceed the propagation speed of the eddy (Flierl, 1981; Chelton et al., 2007, 2011b; Early et al., 2011). Thus we firstly calculated the "trapping depth" separately in the two different periods. The average of the swirl velocity on the edge of the eddy core was computed as the rotational speed of the AE at each level. The propagation speed was the mean value within each period as mentioned in Section 3.1. The vertical profiles of the rotational speed and the mean propagation speed were shown in Fig. 9. The vertical extent of the trapped water volume in the composite AE can reach to 400×10^4 Pa (580×10^4 Pa) in T1 (T2) period. It showed that the trapping depth increased significantly with the AE's westward propagation, which means that the AE can transport much deeper water as it was growing up. Therefore, the water volume trapped within the eddy was estimated by the integrated volume of the eddy core

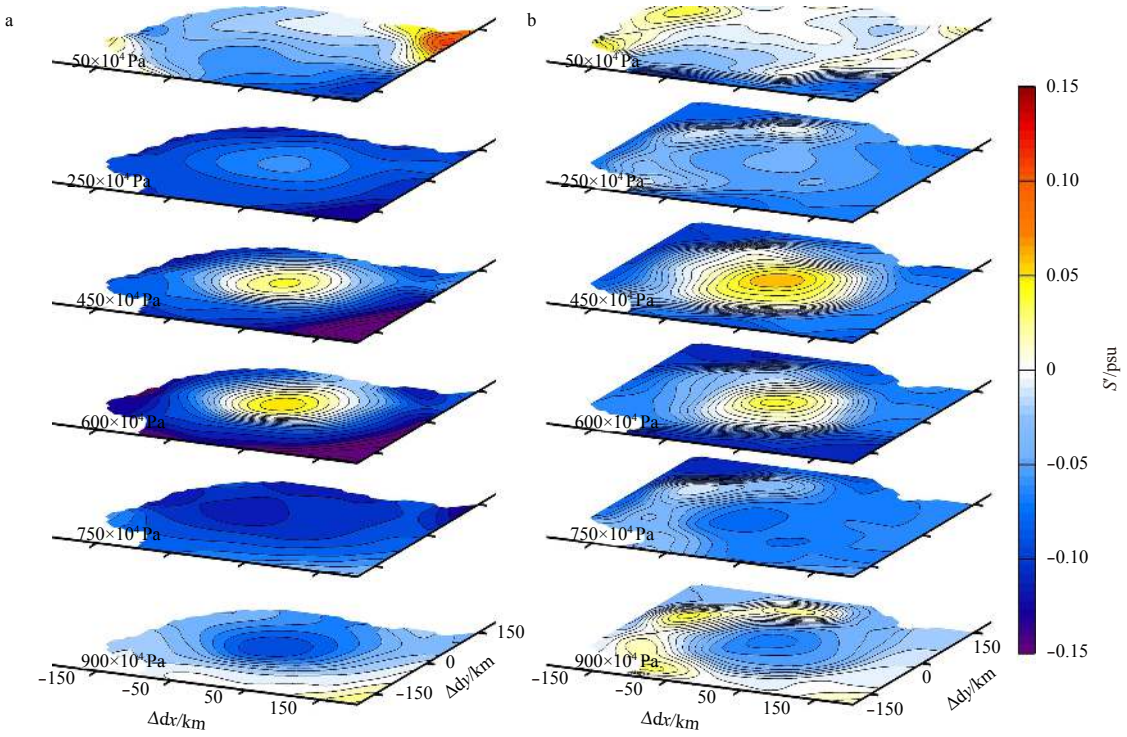

Fig. 6. S' fields (psu) of the composite AE at 50×10^4, 250×10^4, 450×10^4, 600×10^4, 750×10^4 and 900×10^4 Pa during periods T1 (a) to T2 (b). The contour interval is 0.008 and the units of the X-axes (Δdx) and y-axes (Δdy) are both kilometer.

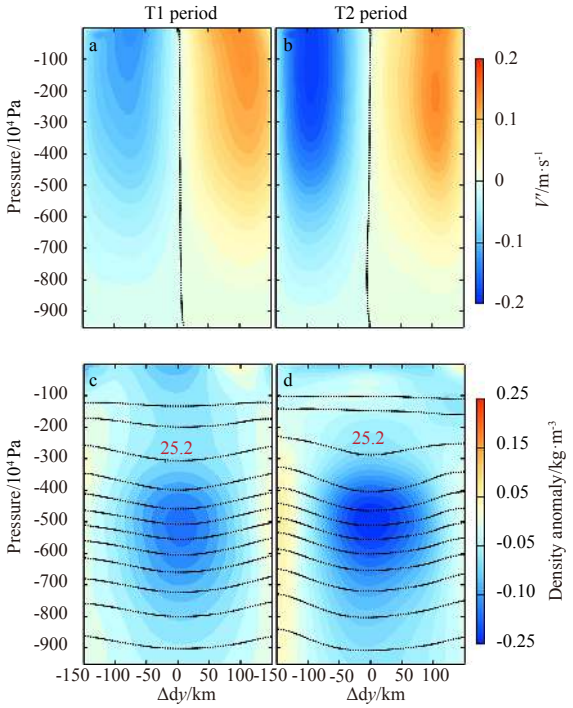

Fig. 7. Vertical sections of the zonal geostrophic current anomaly V' (m/s) of the composite AE at Δdx=0 during T1 (a) and T2 (b) period (The contour interval is 0.01 m/s and the dashed lines indicate the zero contours), and vertical sections of the density (black contours; in kg/m^3) and density anomaly (color shading; in kg/m^3) of the composite AE at Δdx=0 during T1 (c) and (d) period (The black contours' interval is 0.2 kg/m^3).

above the trapping depth, which was about 1.1×10^{13} m^3 (2.2×10^{13} m^3) in T1 (T2) period. Spread over the observation period of nearly four months, the mean westward water volume transport of the AE can be 0.17 $\times10^6$ m^3/s, which was comparable with previous studies of eddy volume transport (Chaigneau et al., 2011).

To estimate how much heat and salt is being transported by AEs, we calculated the available heat and salt content anomalies (AHA and ASA) per meter on the vertical:

$$\mathrm{AHA} = \int \rho C_p T' \mathrm{d}A, \tag{4}$$

$$\mathrm{ASA} = 0.001 \int \rho S' \mathrm{d}A, \tag{5}$$

where ρ is the density (in kg/m^3), C_p is the specific heat capacity (4 000 J·kg/K), and T', S' are integrated over the area (A) of the composite eddy delimited by the ellipse. The factor 0.001 converts salinity to salinity fraction (kg of salt per kg of seawater). Figures 10a and b showed the vertical profiles of AHA and ASA within the composite AE, respectively. It can be clearly seen that both of the AHA and ASA in the eddy growing stage (T2) was larger than growing stage (T1). In the core of the composite AE, maximum AHA was larger than 1.7×10^{17} (2.5×10^{17}) J/m whereas ASA was larger than 0.9×10^9 (1.7×10^9) kg/m during T1 (T2) period. Corresponding to the vertical distribution of S', the negative ASA between 100×10^4 and 350×10^4 Pa was speculated to be related with the subduction of surface freshwater caused by the heavy rainfall (Qu et al., 1999; Li and Wang, 2012). In T1 period, the local maximum AHA and ASA, which was deeper than 400 m, was however not trapped and thus not transported by the AE based on Fig. 9. Integrated from the surface to the trapping depth (400 m for T1 and 580 m for T2), the total available heat and salt content anomalies transported by AE can reach to 3.3×10^{19} J (3.7×10^{19} J) and -2×10^{11} kg (-2.3×10^{10} kg) during T1 (T2) period. Spread over the observation period of nearly four months, the mean anomalies of heat and salt transports of the AE can reach 3.6×10^{11} W and -2.1×10^3 kg/s, respectively. In the study region, previous studies have focused on the regional composite analysis of mesoscale eddies, majorly including eddies' averaged horizontal and vertical structures (Liu et al., 2012; Yang et al., 2013; Sun et al., 2017), the ASA and AHA induced by the eddy were rarely discussed. Compared with other results in different oceans, the observed AE was exceptional with large negative ASA, which usually should be positive values. This was also supposed to be related with the surface freshwater induced by the heavy rainfall.

3.4 *Energy analysis of the AE*

The mean vertical profiles of the EPE and EKE inside the composite AE were shown in Figs 11a and b. Following Oey [2008], the EPE was determined as

$$\mathrm{EPE} = \frac{g^2}{2N^2}\frac{\overline{\rho'^2}}{\rho_0^2}, \tag{6}$$

where N^2 is the square Brunt-V frequency, g is the gravitational acceleration, ρ' is the density anomaly and ρ_0 is the mean density of sea water. The mean vertical distribution of EKE (Fig. 11b) was generally consistent with the distributions of velocity with a notable intensification as the eddy propagated westward. It was found that the either of the maximum of eddy relative vorticity, velocity and EKE were maintained at the sea surface indicative of the strong baroclinicity of the AE. Both of the amplitude of V'(Figs 7a, b) and EKE show slow decay beneath 600×10^4 Pa. However, the EKE showed a rapid reduction from the sea surface to 600 dbar with only 10.6% (14.7%) of EKE left beneath that level in T1 (T2) period. Differently, large values of EPE appeared around the eddy center at 450×10^4–600×10^4 Pa similar to the distribution of density anomaly (Figs 7c, d) and T' (Fig. 11a), which was due to the lifting isopycnals. The fluctuations of the thermocline inside the eddy can be described by the value of EPE to a large extent. The large EPE values of the AE can be regarded the sources of intensified mesoscale activity at subsurface (Roullet et al., 2014)

As the AE propagated westward, it grew from relative weak in March to its strongest in July. The EKE increased greatly from June to July (Fig. 3c). Thus the energy sources of the AE were further examined. According to previous studies, the baroclinic instability (BCI) is the main eddy energy source over most oceans (Stammer, 1997; Wang and Ikeda, 1997; Qiu, 1999). Meantime the background velocity was difficult to determine, which resulted in the barotropic instability cannot be estimated. Therefore, we majorly examined the BCI during the different stages of the eddy growth. Following Oey (2008), the BCI was defined as

$$\mathrm{BCI} = -\frac{g^2}{N^2\rho_0^2}\left(\overline{\rho'u'}\frac{\partial\overline{\rho}}{\partial x} + \overline{\rho'v'}\frac{\partial\overline{\rho}}{\partial y}\right), \tag{7}$$

where the overbar stands for time mean, and the others are

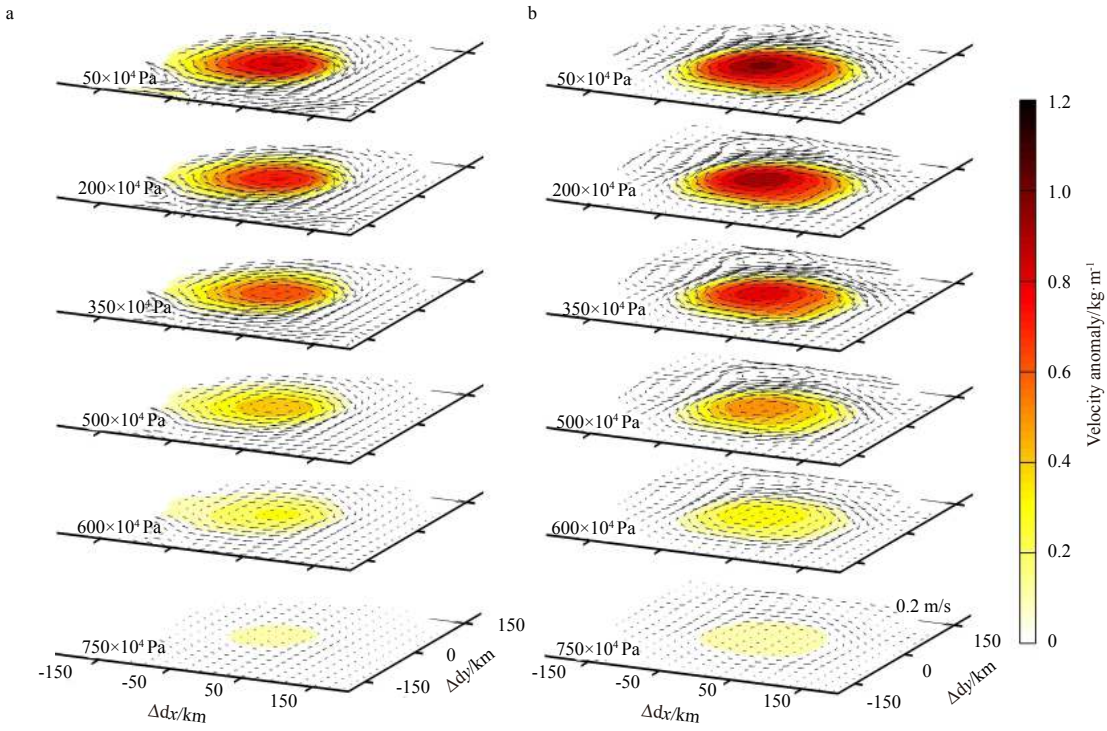

Fig. 8. Horizontal fields of geostrophic velocity anomaly (vectors; in m/s) and DH' (color shading; in m²/s²) of the composite AE during T1 (a) and T2 (b) period. The units of the X-axes (Δdx) and Y-axes (Δdy) are both km.

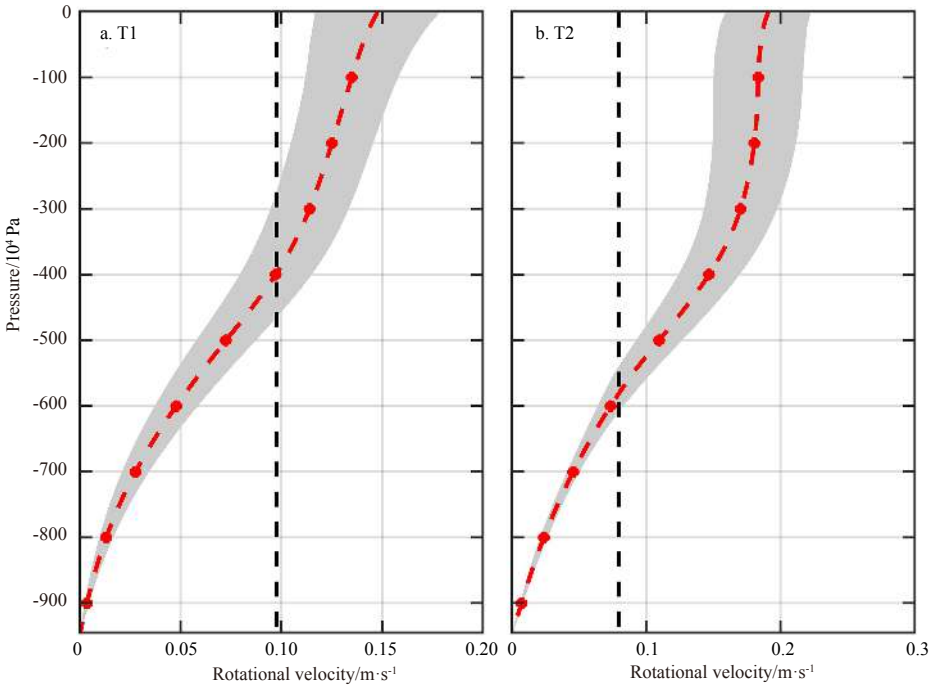

Fig. 9. Vertical profile of the rotational speed of AE (solid line) and its errors (shadings) in T1 (a) and T2 (b) period. The dashed line indicates the mean propagation speed of the AE (0.08 m/s).

standard. If we estimate N^2 from the WOA13 climatology, the BCI of the AE in vertical can be estimated, which was shown in Fig. 11c. It was discernable that the BCI kept positive in whole depth, which indicated the eddy drains energy from the mean available potential energy field. The significant different values of BCI between T1 and T2 period indicated that the AE drained increasing energy from the mean background current through BCI. If we assumed the time difference between T1 and T2 period was 2 months, then the proportion of the energy variance of total eddy energy (TEE, sum of the EKE and EKE) between the two periods associated with BCI can be estimated. The depth-integrated calculation indicated that the BCI can provide 63.8% of the TEE vari-

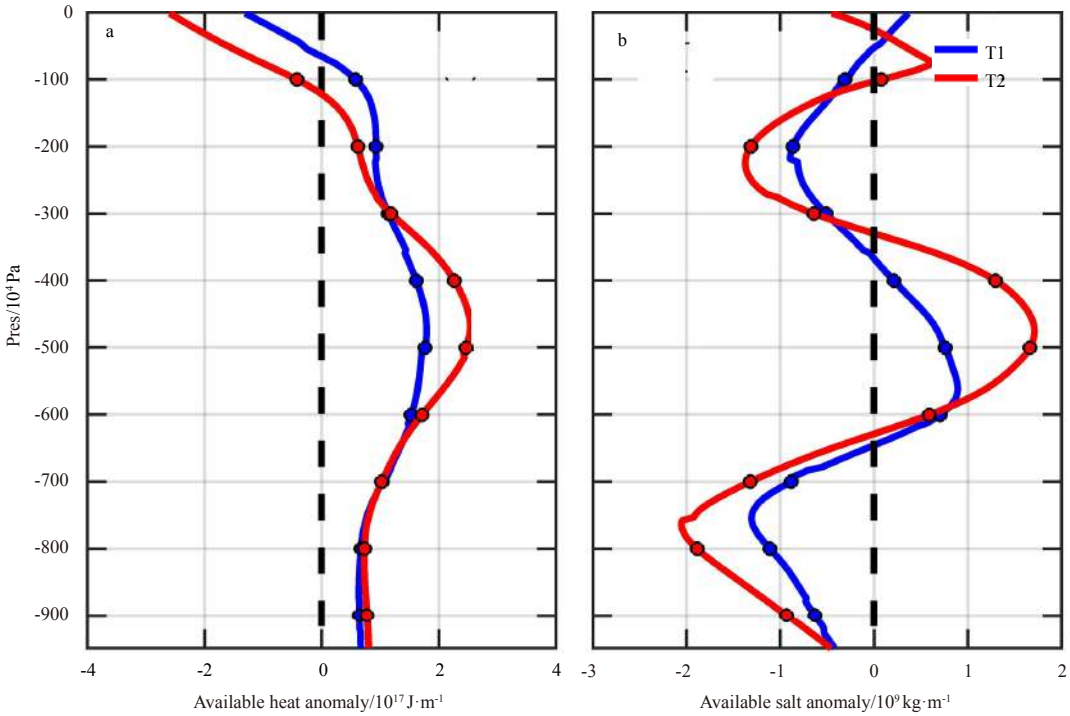

Fig. 10. Mean available heat anomaly (a) and salt anomaly (b) , inside composite AE during period T1 (blue line) and T2 (red line).

ance between T1 and T2 period. Obviously, the BCI was the major source of energy for the growth of the observed AE. This result was consistent with previous studies that the background currents passed energy to the mesoscale eddy which led to the continuing growth of the eddy and the BCI was the main energy source of eddy evolution in the study region (Qiu, 1999). This indicated that the vertical shear of the background currents were more significant than the horizontal shear, during the energy transfer from background currents to mesoscale eddies in the study region.

4 Discussion

The evolutions of the AE detected by SLA and the variations of Argo floats' distributions were shown in Fig. 2. It was discernable that the Argo floats' movements were directly modulated by the AE, which may indicate indirectly the eddy can actually transport the water bolus from remote to the local region. The mean displacement and speed of these Argo floats can reach to 349 km and 13 km/d. At the beginning, 17 Argo floats were intensively deployed in the AE; 11 Argo floats were still trapped at the end of T1 period and only 6 Argo floats remained with others drifted away from the AE at the end of T2 period. The relative distances (r_n) of these 6 Argo floats to the eddy center are shown in Fig. 12a. The r_n was defined as r/R_0, where r is the radial distance from the center of the eddy and R_0 is the radius of the AE identified by the method of Okubo-Weiss. The results showed that the distributions of Argo floats trapped within AE were relative irregularly, being alternating moving far away or close to the eddy center. The relation between Argo floats' distribution and the fluctuations of the isopycnal (26.0 kg/m^3) corresponding to each Argo floats were also examined (Figures not shown). It was found that the fluctuations of the isopycnal and the r_n showed same signs during the whole observation, of which the correlation coefficient reaching 0.65±0.09. This result may indicate that over time the horizontal movements of the Argo floats were related with the eddy-induced vertical fluctuations to some extent, which need further studies with more Argo projects within mesoscale eddies. Furthermore, we statistically defined that if the distance between the Argo float and the eddy center was no less than 1.5 r_n, then this Argo float was thought to be trapped within the AE. Depended on this criterion, the percentage of the remaining trapped Argo floats can be given through the eddy growth (Fig. 12d). It was obviously that the percentage was decreasing as time went on and at last only six Argo floats were still trapped by the AE. Except, during the T1 period, over 80% of the Argo float were trapped within the eddy and the percentage remained constant, but during the T2 period, the percentage rapidly decreased, which is just corresponding to the variation of eddy's radius, amplitude and EKE (Fig. 3). This phenomenon may indicate that the water bolus that initially trapped within the eddy would not maintain all the time during the eddy's growth as a result of water advection or mixing with the surrounding background field. And the intensity of the exchange process of water parcels trapped within the eddy was closely related with the speed of eddy growth.

5 Summary

Based on multi-satellite altimetric SLA and 17 Argo floats (World Meteorological Organization (WMO) IDs 2901550–2901566) *T*/*S* data profiles from March 25 to July 30 in 2014, this study provided a comprehensive description of the three-dimensional structures of an AE in the STNWP. The AE generated near the Kuroshio Extension and propagated westward with mean speed of 8.9 cm/s. The eddy had a lifetime of more than 4 months with the maximum radius of 118 km and maximum SLA reaching 17.7 cm. During the eddy growth, it is found that during the first half, the eddy radius, amplitude and EKE remain stable, but in the second half the eddy begin to grow rapidly. Three-dimen-

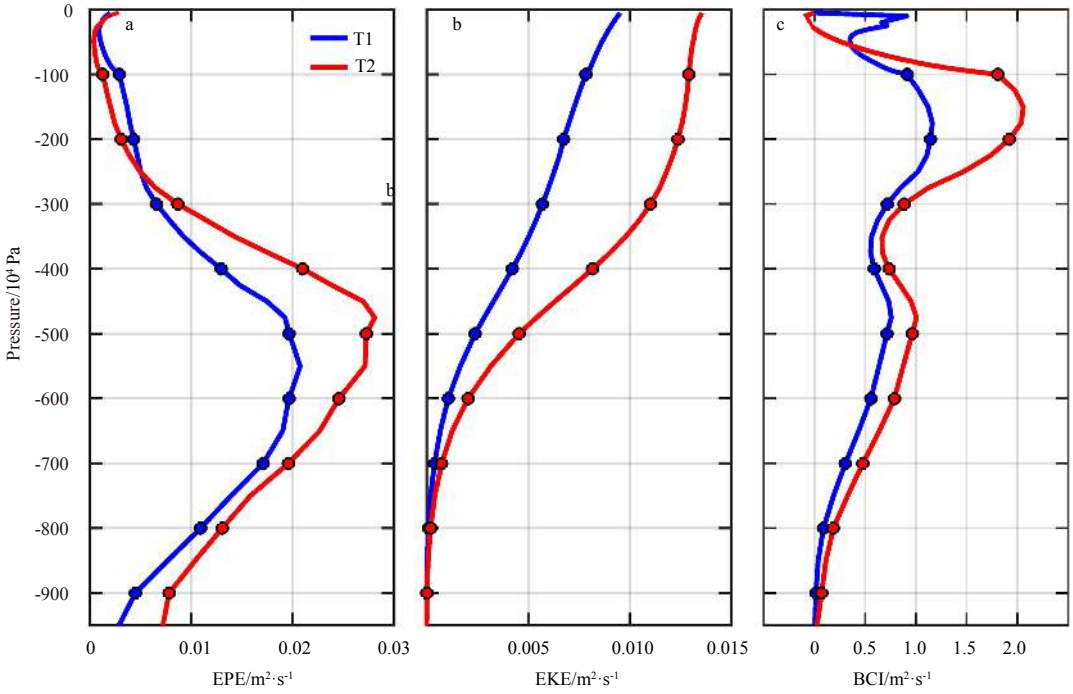

Fig. 11. Mean vertical profiles of the EPE (a), EKE (b) and BCI (C) inside the composite AE during T1 period (blue line) and T2 period (red line).

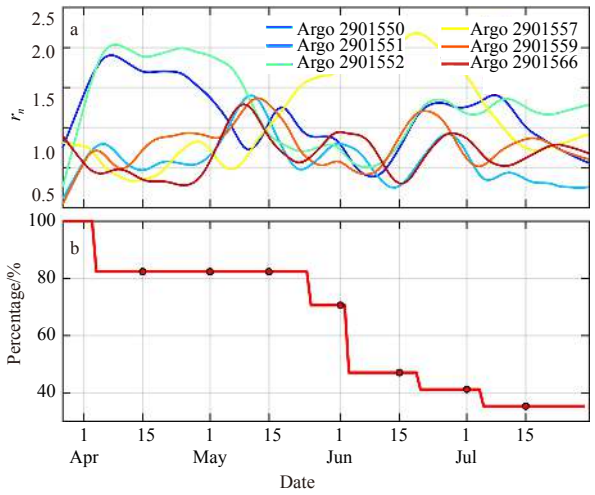

Fig. 12. The relative distances r_n of the last six trapped Argo floats to the center of the AE (a) and the percentage of the remaining trapped Argo floats (b). Different colors represent different Argo floats.

sional structures of an AE were examined through composite analysis in eddy's growing and further growing stage, respectively. The results provided *T*/*S* anomalies, density and velocity images of eddies in detail. The vertical section of the isopycnals showed clearly downward displacements with maximum of 80 cm. The AE exhibited *T*, *S* and density anomalies with maximum reaching 1.7 (1.9)°C, 0.04 (0.07) psu and 0.18 (0.24) kg/m^3 within the eddy core in T1 (T2) period. Corresponding to the concave-down isopycnals, the vertical patterns of the T anomaly were almost positive in the whole depth. Interestingly, the AE showed a sandwich-like S anomaly pattern only with anomalies at 350×10^4–650×10^4 Pa were positive. This structure is probably depended on the vertical distribution of the water mass and the freshwater at sea surface due to the heavy rainfall.

It was discernable that the eddy's influence on the subsurface ocean was even more significant with its growth. The trapping depth increased from 400×10^4 to 580×10^4 Pa, which means that more water volume, heat and salt content in deeper layers can be trapped and transported while it was growing up. In this work, we mainly consider the transport by the observed single eddy. Spread over the observation period of nearly four months, the mean volume flux of water trapped within the AE is about 0.17×10^6 m^3/s. The mean anomalies of heat and salt transports of the AE during the whole observation period are of 3.6×10^{11} W and −2.1×10^3 kg/s, respectively. The AE showed the strongest signal at the surface in terms of the velocity, vorticity and EKE, none of which showed much variation beneath 600×10^4 Pa. But the EKE hugely reduced from surface to 600×10^4 Pa. with only 10.6% (14.7%) of EKE left beneath that level in T1 (T2) period. The positive BCI in almost full depth indicate that it is the main energy source for the eddy growth and based on our calculation the BCI can provide 63.8% of the TEE variance between the two periods. The changing percentage of the remaining trapped Argo floats indicate that the water bolus that initially trapped within the eddy would not maintain all the time during the eddy's growth as a result of water advection or mixing with the surrounding background field. And the intensity of the exchange process of water parcels trapped within the eddy was closely related with the speed of eddy growth.

These results will be helpful for the validation of regional models and investigation the relations between ecosystems and eddies. In turn, regional models could help us explain the exact mechanisms of the eddy formation and dissipation and estimate the eddy-induced transport more precisely.

Acknowledgements

We thank the captain and crew of R/V *Dongfanghong 2* for executing the P-MoVE. All the Argo data used in the article are available on the website (http://www.usgodae.org).

References

Chaigneau A, Gizolme A, Grados C. 2008. Mesoscale eddies off Peru in altimeter records: Identification algorithms and eddy spatio-temporal patterns. Progress in Oceanography, 79(2–4): 106–119, doi: 10.1016/j.pocean.2008.10.013

Chaigneau A, Le Texier M, Eldin G, et al. 2011. Vertical structure of mesoscale eddies in the eastern South Pacific Ocean: a composite analysis from altimetry and Argo profiling floats. Journal of Geophysical Research, 116(C11): C11025, doi: 10.1029/2011JC007134

Chelton D B, Gaube P, Schlax M G, et al. 2011a. The influence of nonlinear mesoscale eddies on near-surface oceanic chlorophyll. Science, 334(6054): 328–332, doi: 10.1126/science.1208897

Chelton D B, Schlax M G, Samelson R M, et al. 2007. Global observations of large oceanic eddies. Geophysical Research Letters, 34(15): L15606, doi: 10.1029/2007GL030812

Chelton D B, Schlax M G, Samelson R M. 2011b. Global observations of nonlinear mesoscale eddies. Progress in Oceanography, 91(2): 167–216, doi: 10.1016/j.pocean.2011.01.002

Chen Gengxin, Gan Jianping, Xie Qiang, et al. 2012. Eddy heat and salt transports in the South China Sea and their seasonal modulations. Journal of Geophysical Research, 117(C5): C05021, doi: 10.1029/2011JC007724

Chu Xiaoqing, Xue Huijie, Qi Yiquan, et al. 2014. An exceptional anticyclonic eddy in the South China Sea in 2010. Journal of Geophysical Research, 119(2): 881–897, doi: 10.1002/2013JC009314

Early J J, Samelson R M, Chelton D B. 2011. The evolution and propagation of quasigeostrophic ocean Eddies. Journal of Physical Oceanography, 41(8): 1535–1555, doi: 10.1175/2011JPO4601.1

Flierl G R. 1981. Particle motions in large-amplitude wave fields. Geophysical & Astrophysical Fluid Dynamics, 18(1–2): 39–74, doi: 10.1080/03091928108208773

Hu Jianyu, Zheng Quanan, Sun Zhenyu, et al. 2012. Penetration of nonlinear Rossby eddies into South China Sea evidenced by cruise data. Journal of Geophysical Research, 117(C3): C03010, doi: 10.1029/2011JC007525

Jing Zhao, Wu Lixin, Li Lei, et al. 2011. Turbulent diapycnal mixing in the subtropical northwestern Pacific: spatial-seasonal variations and role of eddies. Journal of Geophysical Research, 116(C10): C10028, doi: 10.1029/2011JC007142

Li Yuanlong, Wang Fan. 2012. Spreading and salinity change of North Pacific Tropical Water in the Philippine Sea. Journal of Oceanography, 68(3): 439–452, doi: 10.1007/s10872-012-0110-3

Li Yuanlong, Wang Fan, Sun Yan. 2012. Low-frequency spiciness variations in the tropical Pacific Ocean observed during 2003-2012. Geophysical Research Letters, 39(23): L23601, doi: 10.1029/2012GL053971

Li Cheng, Zhang Zhiwei, Zhao Wei, et al. 2017. A statistical study on the subthermocline submesoscale eddies in the northwestern Pacific Ocean based on Argo data. Journal of Geophysical Research, 122(5): 3586–3598

Liang Junhong, McWilliams J C, Kurian J, et al. 2012. Mesoscale variability in the northeastern tropical Pacific: Forcing mechanisms and eddy properties. Journal of Geophysical Research, 117(C7): C07003, doi: 10.1029/2012JC008008

Liu Yu, Dong Changming, Guan Yuping, et al. 2012. Eddy analysis in the subtropical zonal band of the North Pacific Ocean. Deep Sea Research Part I: Oceanographic Research Papers, 68: 54–67, doi: 10.1016/j.dsr.2012.06.001

Morrow R, Fang Fangxin, Fieux M, et al. 2003. Anatomy of three warm-core Leeuwin current eddies. Deep Sea Research Part II: Topical Studies in Oceanography, 50(12–13): 2229–2243, doi: 10.1016/S0967-0645(03)00054-7

Noh Y, Yim B Y, You S H, et al. 2007. Seasonal variation of eddy kinetic energy of the North Pacific Subtropical Countercurrent simulated by an eddy-resolving OGCM. Geophysical Research Letters, 34(7): L07601, doi: 10.1029/2006GL029130

Oey L Y. 2008. Loop current and deep eddies. Journal of Physical Oceanography, 38(7): 1426–1449, doi: 10.1175/2007JPO3818.1

Okubo A. 1970. Horizontal dispersion of floatable particles in the vicinity of velocity singularities such as convergences. Deep Sea Research and Oceanographic Abstracts, 17(3): 445–454, doi: 10.1016/0011-7471(70)90059-8

Qiu Bo. 1999. Seasonal eddy field modulation of the North Pacific Subtropical Countercurrent: TOPEX/Poseidon observations and theory. Journal of Physical Oceanography, 29(10): 2471–2486, doi: 10.1175/1520-0485(1999)029<2471:SEFMOT>2.0.CO;2

Qiu Bo, Chen Shuiming. 2005. Eddy-induced heat transport in the subtropical North Pacific from Argo, TMI, and altimetry measurements. Journal of Physical Oceanography, 35(4): 458–473, doi: 10.1175/JPO2696.1

Qiu Bo, Chen Shuiming. 2010. Interannual variability of the North Pacific Subtropical Countercurrent and its associated mesoscale eddy field. Journal of Physical Oceanography, 40(1): 213–225, doi: 10.1175/2009JPO4285.1

Qiu Bo, Chen Shuiming. 2013. Concurrent decadal mesoscale eddy modulations in the western North Pacific subtropical gyre. Journal of Physical Oceanography, 43(2): 344–358, doi: 10.1175/JPO-D-12-0133.1

Qu Tangdong, Mitsudera H, Yamagata T. 1999. A climatology of the circulation and water mass distribution near the Philippine Coast. Journal of Physical Oceanography, 29(7): 1488–1505, doi: 10.1175/1520-0485(1999)029<1488:ACOTCA>2.0.CO;2

Rio M H, Schaeffer P, Moreaux G, et al. 2009. A new mean dynamic topography computed over the global ocean from GRACE data, altimetry and *in-situ* measurements. In: OceanObs'09 Conference Proceedings. Venice: IOC/UNESCO and ESA, vol. 25.

Roemmich D, Gilson J. 2001. Eddy transport of heat and thermocline waters in the North Pacific: a key to interannual/decadal climate variability?. Journal of Physical Oceanography, 31(3): 675–687, doi: 10.1175/1520-0485(2001)031<0675:ETOHAT>2.0.CO;2

Roullet G, Capet X, Maze G. 2014. Global interior eddy available potential energy diagnosed from Argo floats. Geophysical Research Letters, 41(5): 1651–1656, doi: 10.1002/2013GL059004

Rudnick D L, Jan S, Centurioni L, et al. 2011. Seasonal and mesoscale variability of the Kuroshio near its origin. Oceanography, 24(4): 52–63, doi: 10.5670/oceanog.2011.94

Sasaki Y N, Schneider N, Maximenko N, et al. 2010. Observational evidence for propagation of decadal spiciness anomalies in the North Pacific. Geophysical Research Letters, 37(7): L07708, doi: 10.1029/2010GL042716

Stammer D. 1997. Global characteristics of ocean variability estimated from regional TOPEX/Poseidon altimeter measurements. Journal of Physical Oceanography, 27(8): 1743–1769, doi: 10.1175/1520-0485(1997)027<1743:GCOOVE>2.0.CO;2

Suga T, Kato A, Hanawa K. 2000. North Pacific Tropical Water: Its climatology and temporal changes associated with the climate regime shift in the 1970s. Progress in Oceanography, 47(2-4): 223–256, doi: 10.1016/S0079-6611(00)00037-9

Sun Wenjin, Dong Changming, Wang Ruyun, et al. 2017. Vertical structure anomalies of oceanic eddies in the Kuroshio Extension region. Journal of Geophysical Research, 122(2): 1476–1496

Talley L D. 1993. Distribution and formation of North Pacific intermediate water. Journal of Physical Oceanography, 23(3): 517–537, doi: 10.1175/1520-0485(1993)023<0517:DAFONP>2.0.CO;2

Wang Jia, Ikeda M. 1997. Diagnosing ocean unstable baroclinic waves and meanders using the quasigeostrophic equations and Q-Vector method. Journal of Physical Oceanography, 27(6): 1158–1172, doi: 10.1175/1520-0485(1997)027<1158:DOUBWA>2.0.CO;2

Wang Jia, Jin Meibing, Patrick E V, et al. 2001. Numerical simulations of the seasonal circulation patterns and thermohaline struc-

tures of Prince William Sound, Alaska. Fisheries Oceanography, 10(S1): 132–148

Weiss J. 1991. The dynamics of enstrophy transfer in two-dimensional hydrodynamics. Physica D: Nonlinear Phenomena, 48(2–3): 273–294, doi: 10.1016/0167-2789(91)90088-Q

Wunsch C. 1999. Where do ocean eddy heat fluxes matter?. Journal of Geophysical Research, 104(C6): 13235–13249, doi: 10.1029/1999JC900062

Xie Shangping. 2013. Advancing climate dynamics toward reliable regional climate projections. Journal of Ocean University of China, 12(2): 191–200, doi: 10.1007/s11802-013-2277-7

Xiu Peng, Chai Fei, Xue Huijie, et al. 2012. Modeling the mesoscale eddy field in the Gulf of Alaska. Deep Sea Research Part I: Oceanographic Research Papers, 63: 102–117, doi: 10.1016/j.dsr.2012.01.006

Xu Lixiao, Li Peiliang, Xie Shangping, et al. 2016. Observing mesoscale eddy effects on mode-water subduction and transport in the North Pacific. Nature Communications, 7(1): 10505, doi: 10.1038/ncomms10505

Yang Guang, Wang Fan, Li Yuanlong, et al. 2013. Mesoscale eddies in the northwestern subtropical Pacific Ocean: statistical characteristics and three-dimensional structures. Journal of Geophysical Research, 118(4): 1906–1925, doi: 10.1002/jgrc.20164

Yoshida S, Qiu Bo, Hacker P. 2011. Low-frequency eddy modulations in the Hawaiian Lee Countercurrent: observations and connection to the Pacific Decadal Oscillation. Journal of Geophysical Research, 116(C12): C12009, doi: 10.1029/2011JC007286

Yuan Dongliang, Wang Zheng. 2011. Hysteresis and dynamics of a western boundary current flowing by a gap forced by impingement of mesoscale eddies. Journal of Physical Oceanography, 41(5): 878–888, doi: 10.1175/2010JPO4489.1

Zhang Dongxiao, Lee T N, Johns W E, et al. 2001. The Kuroshio east of Taiwan: modes of variability and relationship to interior ocean mesoscale eddies. Journal of Physical Oceanography, 31(4): 1054–1074, doi: 10.1175/1520-0485(2001)031<1054:TKEOTM>2.0.CO;2

Zhang Zhiwei, Li Peiliang, Xu Lixiao, et al. 2015. Subthermocline eddies observed by rapid‐sampling Argo floats in the subtropical northwestern Pacific Ocean in Spring 2014. Geophysical Research Letters, 42(15): 6438–6445, doi: 10.1002/2015GL064601

Zhang Zhiwei, Liu Zhiyu, Richards K, et al. 2019. Elevated diapycnal mixing by a subthermocline eddy in the western equatorial Pacific. Geophysical Research Letters, 46(5): 2628–2636, doi: 10.1029/2018GL081512

Zhang Zhiwei, Tian Jiwei, Qiu Bo, et al. 2016. Observed 3D structure, generation, and dissipation of oceanic mesoscale eddies in the South China Sea. Scientific Reports, 6(1): 24349, doi: 10.1038/srep24349

Zhang Zhiwei, Zhao Wei, Tian Jiwei, et al. 2013. A mesoscale eddy pair southwest of Taiwan and its influence on deep circulation. Journal of Geophysical Research, 118(12): 6479–6494, doi: 10.1002/2013JC008994

Zhang Ronghua, Rothstein L M, Busalacchi A J. 1998. Origin of upper-ocean warming and El Niño change on decadal scales in the tropical Pacific Ocean. Nature, 391(6670): 879–883, doi: 10.1038/36081

Zhang Zhengguang, Wang Wei, Qiu Bo. 2014. Oceanic mass transport by mesoscale eddies. Science, 345(6194): 322–324, doi: 10.1126/science.1252418

Zheng Quanan, Lin Hui, Meng Junmin, et al. 2008. Sub-mesoscale ocean vortex trains in the Luzon Strait. Journal of Geophysical Research, 113(C4): C04032, doi: 10.1029/2007JC004362

Zheng Quanan, Tai Changkuo, Hu Jianyu, et al. 2011. Satellite altimeter observations of nonlinear Rossby eddy-Kuroshio interaction at the Luzon Strait. Journal of Oceanography, 67(4): 365–376, doi: 10.1007/s10872-011-0035-2